MULTISCALE FUSION OF INSAR DATA FOR HYDROLOGICAL APPLICATIONS

K. Clint Slatton, Larry Teng, and Melba Crawford

The Center for Space Research, The University of Texas at Austin
3925 W. Braker Ln., Suite 200, Austin, TX 78759 USA
Austin, TX 78712-1084 USA
{slatton, teng, crawford}@csr.utexas.edu

Abstract - Accurate determination of topography is required for a wide range of civilian and governmental applications. For example, modeling flood extent, flow velocity, and sediment transport associated with river networks requires bare-surface elevations with sub-meter height accuracy and spatial resolutions better than 10 meters. Strip-map interferometric synthetic aperture radar (INSAR) sensors have been used extensively to map topography. However, most INSAR data have insufficient spatial resolution and height accuracy for high-resolution flood modeling.

We combine space-borne INSAR data from the ERS-1/2 platforms with multiple sets of airborne C-band INSAR data acquired by the NASA/JPL TOPSAR platform to obtain statistically optimal high-resolution estimates of topography over the Finke River Gorge in central Australia. We fuse the INSAR data using a multiscale Kalman smoothing approach. The estimated topography preserves the spatial resolution of the TOPSAR data while smoothing noise and providing estimates where there was no TOPSAR coverage.

1. INTRODUCTION

Understanding and quantifying hydrological processes associated with floods, water runoff, and sediment transport are critical in preparing for and mitigating natural disasters and managing land use. Modeling such hydrological process requires detailed knowledge of the topography. This information is typically provided in the form of a Digital Elevation Model (DEM). Strip-map INSAR technology is well-suited to mapping topography over large regions such as a water drainage network and associated river channels. However, the spatial resolutions needed for hydrological modeling typically require airborne INSAR data, which can suffer from radar shadowing and foreshortening in areas with high relief. Also, the height uncertainty of these INSAR measurements is typically greater than 1 meter. Errors of this magnitude can be significant because detailed cross sections of run-off and river channels are extracted from the DEMs for use in the hydrological models [11].

We examine INSAR data over the Finke River in Australia. The Finke River Gorge is an ancient river system in arid Central Australia that flows between two mountain ranges, and crosses through intervening pediments and plains. It has served as a long term study site for paleohydrology and relict vegetation studies. An overview of the region is shown in Fig. 1. The figure consists of a large-scale AUSLIG DEM with the locations of INSAR data acquired by the ERS and TOPSAR systems indicated. The TOPSAR acquisitions are referenced by the flight line targets. Single flight lines were acquired over Palm Valley and Ellery Creek, while two were acquired over the Finke River.

Figures 2 and 3 show the INSAR DEMs used in this work. The height uncertainty σ_h for each DEM was computed from the coherence image [1]. The ERS data were acquired in 1996 (tandem pair, baseline = 136 m), a single TOPSAR flight line was flown over the Finke Gorge during the 1996 PacRim mission, and three TOPSAR flight lines were acquired in 2000, as part of the PacRim 2000 TOPSAR deployment. Missing data caused by radar shadowing, unwrapping errors, and low backscatter targets can be seen in each line, but were particularly prevalent in the high resolution DEMs acquired in 2000. We examine the region of overlap of these data acquisitions to investigate the impact of multiple acquisitions on DEM quality.

Multiscale, or hierarchical, signal modeling has received much attention over the last ten years. The work has been motivated primarily by the need to develop stochastic models that capture the true multiscale character of many natural processes and a need to combine signals and process measurements of differing resolutions (data fusion). Approaches to

This work was supported by the National Aeronautics and Space Administration, under the Topography and Surface Change Program (Grant NAG5-2954, NAG5-7660) and the Graduate Student Research Fellowship Program (Grant NGT-50239) and the Army Research Office, under the Terrestrial Sciences Program (DAAG55-98-1-0287).

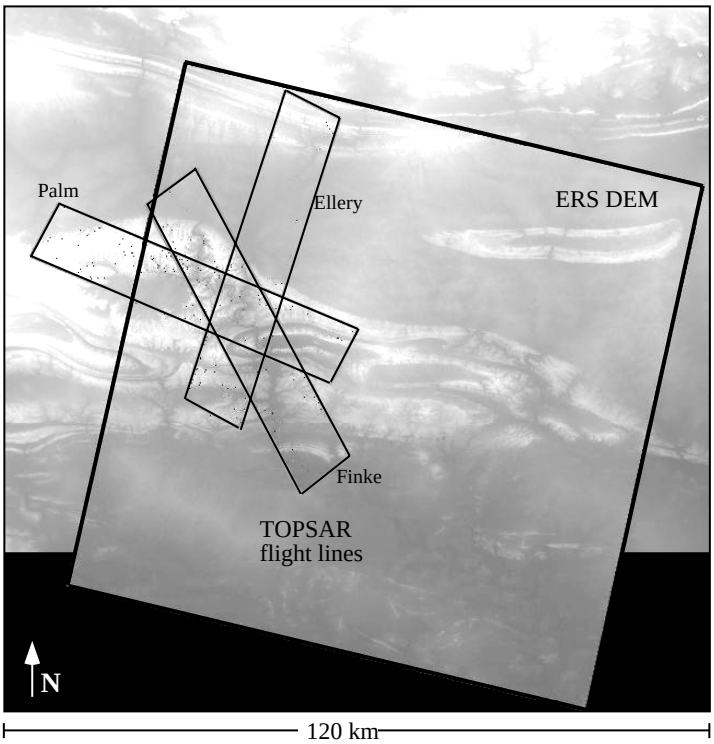

Fig. 1. Overview of the Finke River and surrounding area in an AUSLIG 9 second DEM. ERS and TOPSAR data were acquired over the Finke River Gorge. Individual TOPSAR acquisitions are indicated by target name.

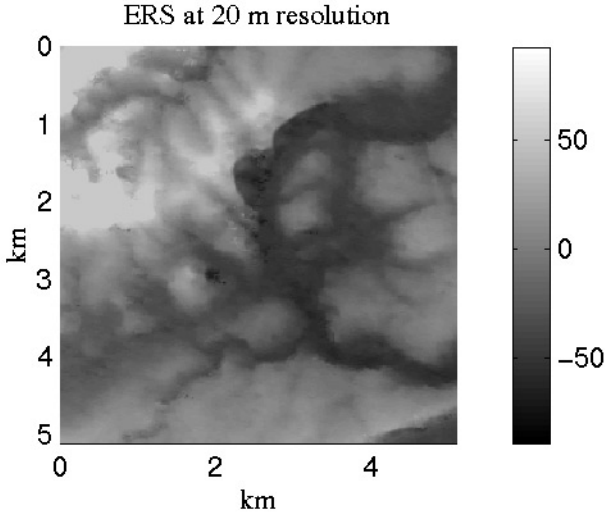

Fig. 2. ERS DEM in the overlap region of the TOPSAR acquisitions shown in Fig. 1.

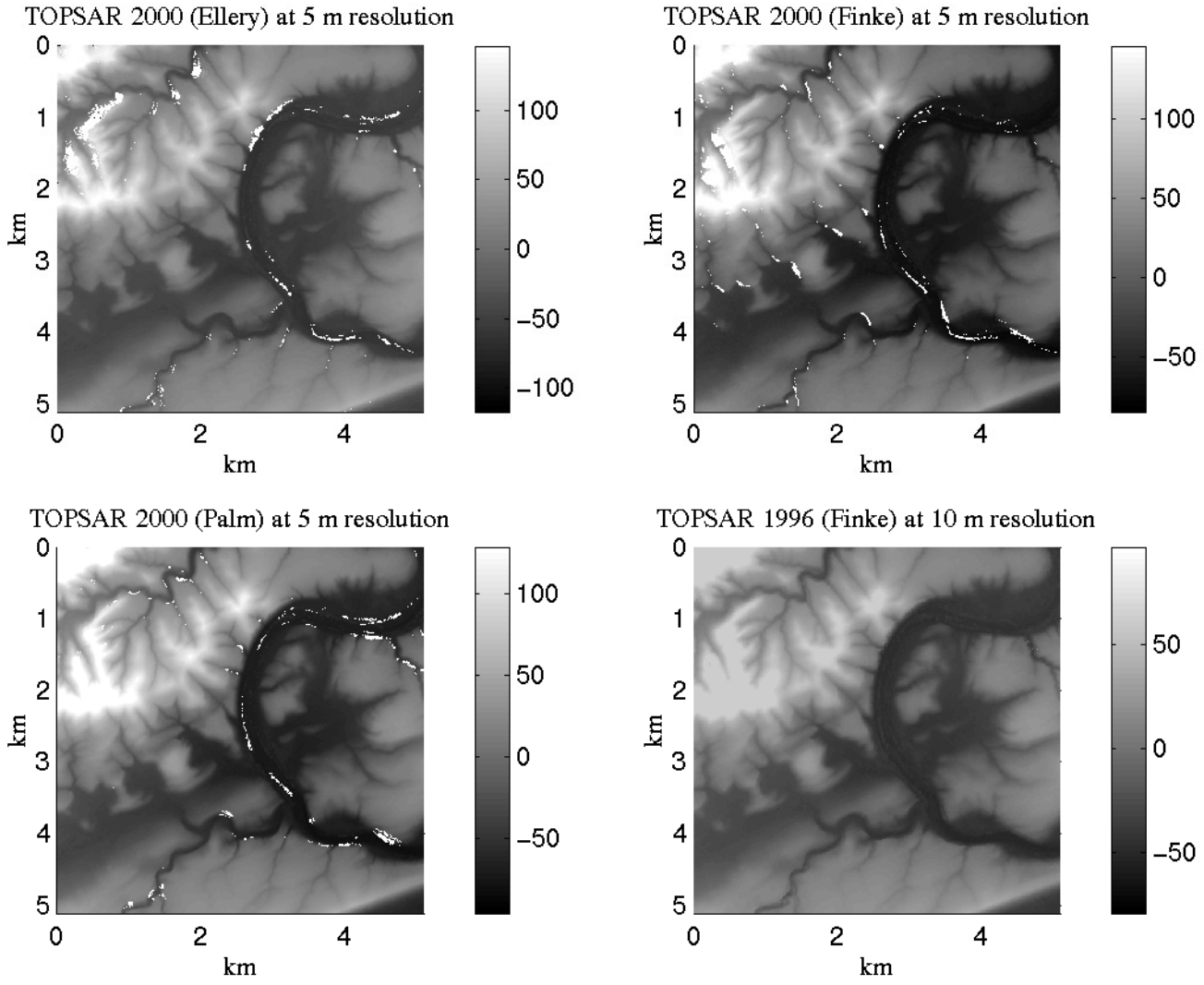

Fig. 3. TOPSAR DEMs in the overlap region of the TOPSAR acquisitions shown in Fig. 1. Missing data can be seen in the three acquisitions from 2000.

hierarchical data modeling have included methods based on fine-to-coarse transformations of spatial models and methods that directly model processes on multiscale data structures, such as dyadic trees or quadtrees [2]. The work reported here uses quadtrees to combine INSAR data of disparate resolutions. A multiscale estimation framework can be useful in many remote sensing applications since multiple data sets of different resolutions are often needed to characterize the processes under study. Chou, *et. al* [3] developed a multiscale linear estimation method based on the Kalman filter. Kumar [4] applied this method to the problem of combining soil moisture data at different resolutions, while other investigators used the method for data interpolation and fusion [5] [6]. They either assumed a linear relationship between the measurements and the state variables or linearized the process equations.

We describe the fusion algorithm in Section 2. In Section 3 we present results of fusing TOPSAR data over the Finke River acquired during the PacRim 2000 campaign. We use the improved DEM to detect changes in the fluvial structure of the river channel in Section 4 and present conclusions in Section 5.

2. MULTISCALE DATA FUSION

The Kalman filter is a linear, time-varying filter that provides optimal estimates, in the mean squared sense, of a stochastic process given a set of observations. The estimates and estimate covariances are both computed in the filter algorithm so that an uncertainty measure is available for each estimate. The Kalman filter inversely weights each estimate by the covariance of the state process (signal model) and the covariance of the observations. Missing data are easily handled because the estimate simply degenerates to a state propagation. Each estimate is a minimum mean squared error (MMSE) estimate conditioned on the most recent observation. MMSE estimates conditioned on all of the observations are obtained by making a return sweep through the data. This subsequent filter is referred to as a Kalman smoother. For background on the Kalman filter, see [10].

The multiresolution Kalman smoother is specified on a quadtree. A multiscale stochastic process is specified by a downward propagating linear dynamic model [3]. Then, using initial conditions at the root node, a realization of the stochastic process is generated with the downward model. A corresponding upward model is defined that is tracked by the multiscale Kalman filter. A complete description of the MKS algorithm can be found in [3] [5]. Using the scalar form for clarity, we have

Downward model:

$$\begin{aligned} x(s) &= \Phi(s)x(Bs) + \Gamma(s)w(s) \quad \forall s \in \mathcal{S}, s \neq 1 \\ y(s) &= H(s)x(s) + v(s) \qquad \forall s \in \mathcal{T} \subseteq \mathcal{S} \end{aligned} \tag{1}$$

Here, x is the state variable, and y represents the observations. The stochastic forcing function w is a Gaussian white noise process with identity variance, and the measurement error v is a Gaussian white noise process with scale dependent variance $R(s)$. $\mathcal{S}$ represents the set of all nodes on the quadtree, and $\mathcal{T}$ denotes those nodes at which an observation is available. s is the node index on the tree, where $s = 1$ denotes the root node. B is a backshift operator in scale, such that Bs is one scale coarser than s. Φ is the coarse-to-fine state transition operator, Γ is the stochastic detail scaling function, H is the measurement-state model, and R represents the measurement variance of the observations.

Initial values for the state estimate and the estimation error variance must be specified to start the Kalman filter algorithm.

Initial conditions:

$$\begin{aligned} \hat{x}_{1|0} &= E[x(1)] = 0 \\ P_{1|0} &= E[x(1)x^T(1)] = P_s(1) \end{aligned} \tag{2}$$

Here, $P_s(s)$ denotes the covariance of the state at node s. The upward model is then specified

Upward model:

$$x(Bs) = F(s)x(s) + \overline{w}(s) \tag{3}$$

$$y(s) = H(s)x(s) + v(s) \tag{4}$$

$$F(s) = P_s(Bs)\Phi^T(s)P_s^{-1}(s) \tag{5}$$

$$\begin{aligned} E[\overline{w}(s)\overline{w}^T(s)] &= P_s(Bs) \cdot \\ &\quad [I - \Phi^T(s)P_s^{-1}(s)\Phi(s)P_s(Bs)] \\ &= Q(s) \end{aligned} \tag{6}$$

Here, F is the fine-to-coarse state transition operator. Q is the process noise covariance in the upward model. It is the multiscale analog to Q in the temporal Kalman filter.

For a 2-D process, MKS algorithm begins with a fine-to-coarse sweep up the quadtree that is analogous to Kalman filtering with an added merge step. This is followed by a coarse-to-fine sweep down the quadtree that corresponds to Kalman smoothing. This algorithm is noniterative and has constant computational complexity per pixel with $\mathcal{O}(\mathcal{S}_M)$ operations, where $\mathcal{S}_M$

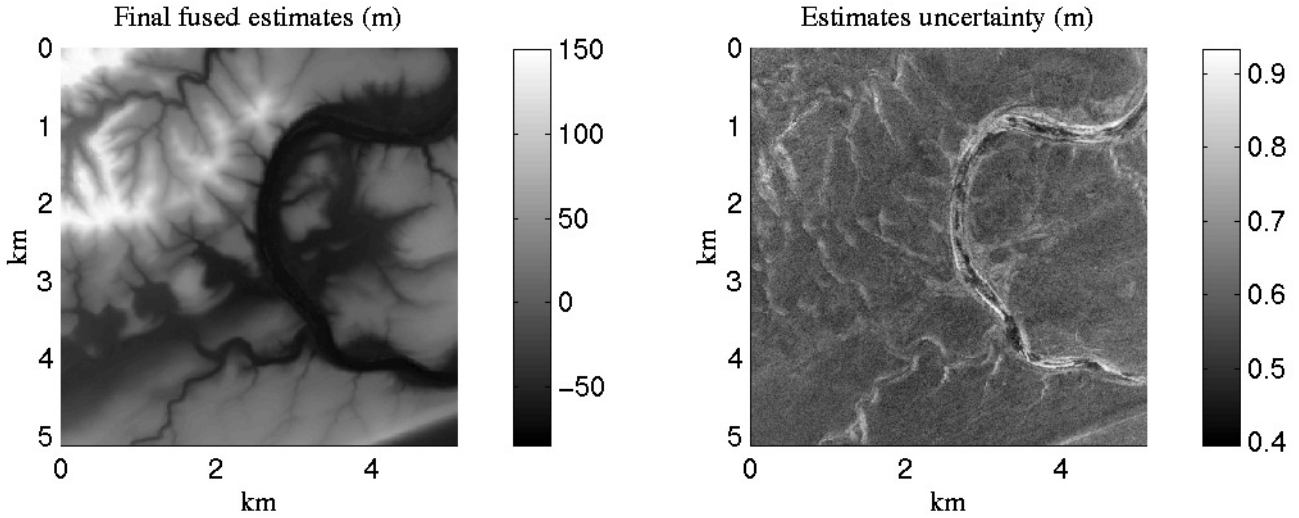

Fig. 4. Final fused DEM estimates and estimate uncertainty.

is the number of nodes at the finest scale $m = M$. Before the MKS algorithm can be applied to the data, a general form for the stochastic model in (1) must be chosen that approximates the scale-to-scale evolution of the state process. Once a general form is selected, specific values for the model parameters $\{\Phi, \Gamma, H, R\}$ must be derived. Because the nonlinear dependence of the observations on the state are accounted for in the transformation of the data, the transformed data can be considered to be noisy estimates of the state. Therefore H is simply a binary indicator function. $H = 1$ at pixels where data are present, and $H = 0$ otherwise.

The measurement error variance R is determined from sensor parameters and from the data. In the case of INSAR data, the Cramer-Rao bound for the phase noise is used to determine a spatially-varying $R(s)$.

$$R(s) \quad = \quad R_{INSAR} \quad \forall s \in \mathcal{T}S \subseteq \mathcal{T} \tag{7}$$

Here, $\mathcal{T}S$ is the set of nodes where SAR data are available. Φ and Γ must then be specified. A description of how the Kalman model parameters Φ and Γ are specified is given in Appendix A. The MKS algorithm is presented in Appendix B.

3. ESTIMATED DEM

The MKS fusion algorithm was applied sequentially to the INSAR data acquisitions. The TOPSAR data from one flight line were first fused with the ERS data to provide a dense DEM at 5 m resolution with coverage over the entire test site. The resulting MKS estimates and estimate variances were then used as the *a priori* estimates and estimated variances respectively in the next MKS iteration, where the Kalman filter was applied to a second TOPSAR flight line. The filter was then applied to the third TOPSAR flight line from the 2000 campaign, using the results from the second iteration for the priors. The final fused DEM preserves the high resolution of the TOPSAR data, optimally fills in data dropouts, and reduces the height uncertainty in the DEM via the minimum mean squared error filtering.

Fig. 4 shows the final fused DEM heights and height uncertainty values. Table 1 indicates how the mean uncertainty decreased after each iteration of the MKS algorithm. The final uncertainty is approximately half of the σ_h values from the individual TOPSAR acquisitions. The reduction in local uncertainty is even greater than indicated in Table 1 because pixels corresponding to data dropouts or distortions due to poor viewing angle are significantly improved. Pixels where there is data dropout were not used to compute σ_h. The uncertainty reported for the fusion results is the standard deviation of the Kalman smoother error covariance, $\sqrt{P^s}$. It was computed using all pixels, including locations of data dropouts in the individual TOPSAR acquisitions. The benefits of multiple acquisitions with different viewing angles can be measured quantitatively after each iteration of the fusion algorithm. This process can thus aid in the design of an acquisition campaign. Diversity of viewing angle is critical for areas of high relief to mitigate the impact of shadowing, foreshortening, and low backscatter targets.

Accurate estimation of the topography in river and runoff channels is critical for hydrological studies. Predictions of flow velocities and sediment transport through the drainage network require cross-sectional profiles of the channels [11]. The set of channel cross sections along the river and drainage pathways is a critical input parameter in many hydrological models [11]. Channels must be located and cross sections must be extracted from the DEM as a first step in modeling flow directions and downstream flow accumulation. In flat areas, small DEM errors can result in significant misalignment of the cross sections. In high relief areas, large DEM errors can occur due to shadowing and foreshortening distortions, which vary with viewing

Table 1. Mean height uncertainty for individual and fused DEMs. Mean uncertainty values are the standard deviation of height errors due to phase noise σ_h for individual DEMs and the standard deviation of the Kalman smoother error covariance $\sqrt{P^s}$ for fused DEMs.

quantity	spatial resolution (m)	mean uncertainty (m)
observations		
ERS	20	18
TOPSAR-Ellery	5	1.9
TOPSAR-Finke	5	1.8
TOPSAR-Palm	5	1.6
fused results		
ERS+TOPSAR-Ellery	5	1.1
prior+TOPSAR-Finke	5	0.76
prior+TOPSAR-Palm	5	0.60

angle of the INSAR acquisition. DEMs resulting from fused TOPSAR and ERS data sets offer locally high spatial resolution and reduced height uncertainty and may have a significant impact on the estimates of hydrological parameters.

DEMs of different resolutions capture topographic structures of different scales. For example, a nine second DEM (250 m approximate resolution) was found to be adequate for delineating the 25 year flood plain on the Logan River drainage basin in Queensland Australia [11]. However, the spatial resolution was insufficient for locating river courses accurately, and the height accuracy was insufficient over flat meandering channels and flood plains where small topographic features that confine the flow were missed. The highest resolution DEM available for the study (25 m) was required to map flow accumulations. By fusing DEMs in a multiscale algorithm, we can produce topographic data for a range of spatial resolutions depending on the application requirements.

Although the spatial resolution and height uncertainty of individual TOPSAR acquisitions may be adequate for some hydrological applications, the noise contribution can lead to artificial pits and damming of small channels [11]. These artifacts can have a dramatic impact on the final predicted flow velocities and sediment depositions, and are typically addressed via post-processing the DEMs with morphological filters and smoothing filters. Fusing multiple INSAR acquisitions via the MKS algorithm reduces the noise while preserving high resolution data, thus ameliorating the impact of the artifacts. The fusion algorithm can also incorporate non-SAR data, such as laser altimeter data, if they are available.

Figure 5 shows a portion of the Finke River channel. It is a gray-scale representation of a true color image acquired by the MASTER hyperspectral sensor. The MASTER sensor was carried on the DC-8 platform, along with the TOPSAR sensor, for near coincident acquisition. The contours in the river channel shown in Fig. 5 were derived from the fused DEM. The contours correspond to 2.5 m intervals in elevation. Channel cross sections at transect AB are shown in Fig. 6. In the steep topography of the channel, discrepancies in topography of up to 5 m can be seen among the three TOPSAR acquisitions.

Each TOPSAR acquisition in 2000 contained a significant number of data dropouts and distorted topography in steep gorges due to foreshortening and double bounce scattering. The viewing angle diversity causes these artifacts to occur in different locations in the individual TOPSAR data sets, so the artifacts are greatly reduced after merging the data into a single DEM.

4. CHANGE DETECTION

The Finke River Gorge experienced a significant flood in 1999. Flow and sediment transport increase during periods of flooding. We compared a TOPSAR acquisition over the Finke River from 1996 to the fused DEM produced from TOPSAR data acquired in 2000 to determine what changes could be observed in the INSAR data.

As the Finke River passes through the James Mountain Range, its path is tightly constrained in some places by steep rocky gorges. But in many places, the river forms a meandering channel. In these locations, the river consists of narrow pools and streams embedded in a broad channel that fills during floods, but is otherwise only a small stream. Figure 5 shows a portion of the Finke River channel that exhibits this characteristic. The channel is roughly 400 m across at this location.

It is these meandering channels where changes associated with fluvial processes are expected. Due to the dynamics of flow velocities and sediment transport, meandering channels often form alternating sand bars at bends in the river [12], see Fig. 7. Pools of water and bank erosion occur on the opposite sides of these bends. An example of a meandering channel is seen in the MASTER image in Fig. 5.

Difference images between the 1996 TOPSAR DEM and the fused 2000 DEM reveal that the largest differences generally occur where there is steep topography, corresponding to shadowing and viewing angle distortions. Thus, simple difference images are not useful for isolating fluvial changes. We were able to isolate changes in the river channel using a binary indicator function $\Delta\sigma = \{0, 1\}$ conditioned on both elevation and relative height uncertainty $\sigma_h^{Finke2000}/\sigma_h^{Finke1996}$. Pixels

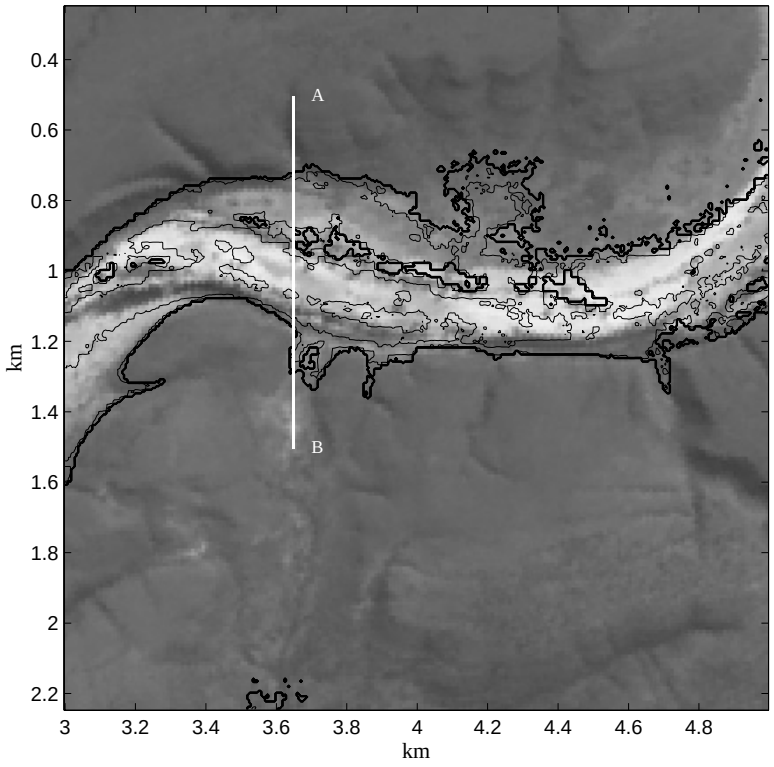

Fig. 5. MASTER optical image overlayed with INSAR contours in the river channel. The contours correspond to 2.5 m elevation increments. The MASTER image has a resolution of 10 m, and the fused DEM has a resolution of 5 m.

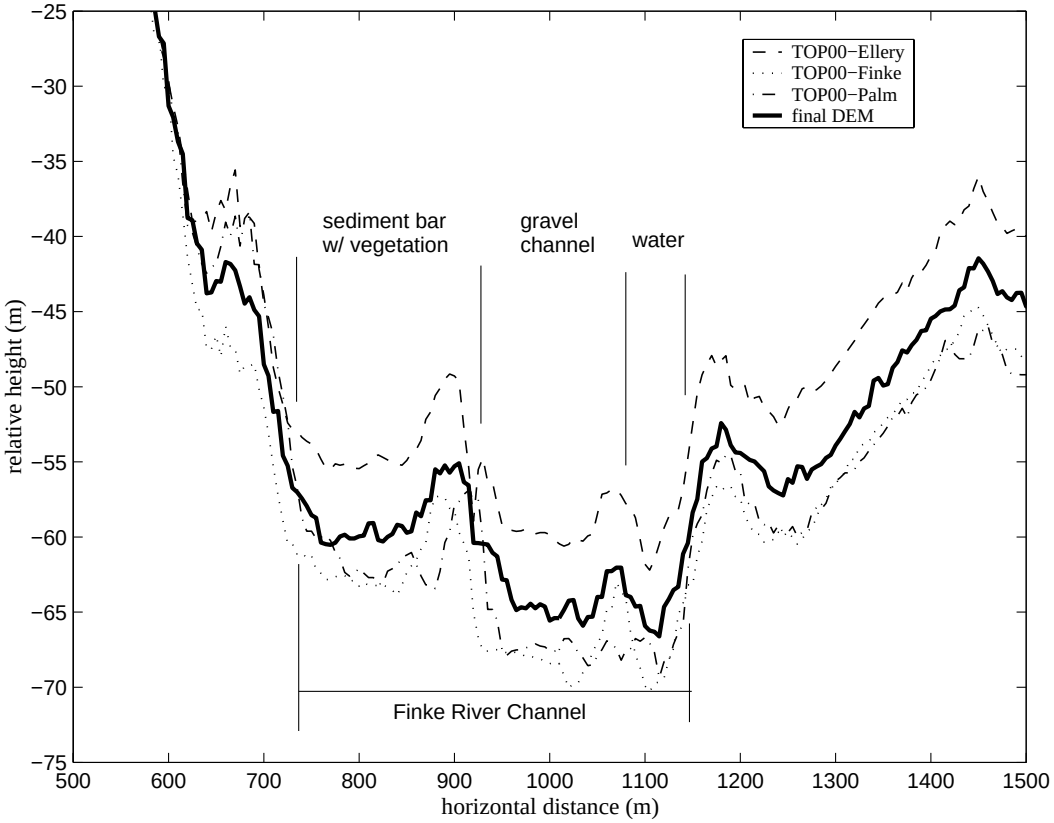

Fig. 6. Channel cross sections extracted from transect AB in the fused DEM in Fig. 5.

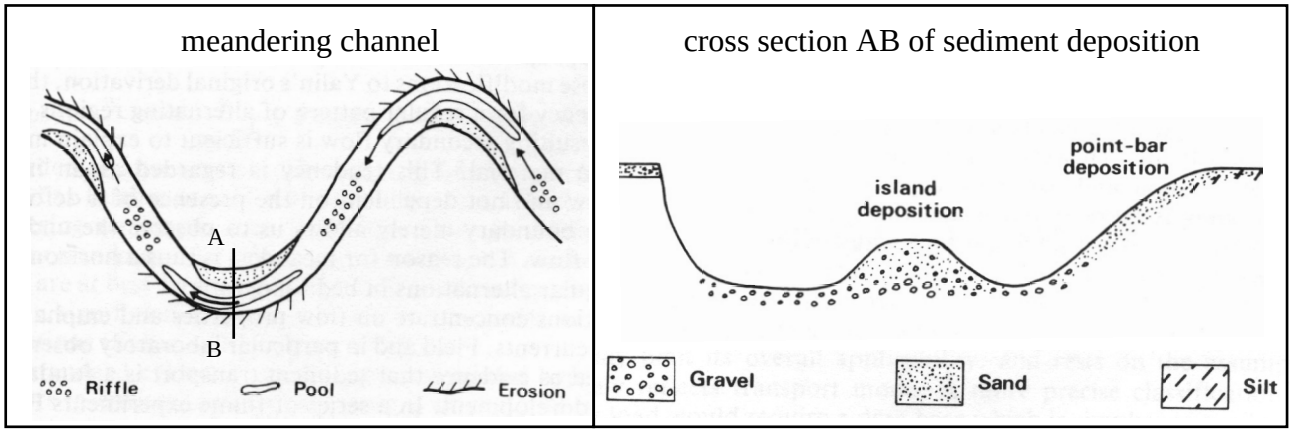

Fig. 7. Anatomy of a meandering channel.

corresponding to low elevations and large changes in the height uncertainty are then considered as candidates for fluvial change in the river channel.

Changes in the channel topography were only on the order of 5 m, but changes in the height uncertainty were large in many places. As a result of the 1999 flood, trees, shrubs, and grasses present in the channel in 1996 may have been swept away. Sediment would have also been redistributed causing changes in surface roughness. Where sediment bars were formed or enlarged, new vegetation may have been established after the flood. All of these processes could cause significant changes in the scattering, and thus in the height uncertainty. Cutoff values for the elevation and height uncertainty ratio used in $\Delta\sigma$ were selected empirically. However, pixels consistent with expected fluvial changes were still successfully isolated for a range of different cutoff values.

Figure 8 shows the isolated pixels and a corresponding transect through the channel in the 1996 DEM and the fused DEM. The overall channel width does not appear to change between 1996 and 2000. This is expected since sandstone hills constrain the main channel on both sides. The channel appears to be approximately level in 1996. In 2000, a sediment bar appears on the north side of the channel, and the south side has dropped 1 to 2 m in elevation.

It appears that the south side of the main channel was scoured between 1996 and 2000 and is now deeper, which is consistent with the evolution of meandering channels. The INSAR coherence images and MASTER optical data indicate that the north-side sediment bar supported vegetation in 2000, and the river only occupied a narrow portion of the south side of the main channel. Our investigation into change detection in the river bed is preliminary. Augmented methods for detecting change using POLSAR and optical data are currently being investigated.

5. CONCLUSIONS

A robust data fusion method was presented and used to combine INSAR data sets acquired from different platforms, at different viewing angles, and at different resolutions. The resulting height uncertainty of the fused DEM is significantly smaller than that of individual INSAR acquisitions, and the reduction in uncertainty as each data set was fused was clearly demonstrated. The fused DEM provides the most dramatic improvement in the steep channels where viewing angle dependent shadowing and foreshortening can severely affect a particular INSAR data set. It may also provide improved mapping of channel cross sections for modeling flow velocities and sediment deposition.

Using the fused DEM from the 2000 PacRim TOPSAR data as a reference, changes in the fluvial structure of the Finke channel occurring between the 1996 and 2000 TOPSAR acquisitions were then mapped. We determined that the change in height uncertainty was a reasonable indicator of fluvial change. We also found evidence of significant structural changes in the point bars and pools of the meandering channel portions of the Finke River gorge.

6. ACKNOWLEDGEMENTS

The authors would like to thank Dr. Geoff Pickup of the Commonwealth Scientific and Industrial Research Organization (CSIRO) in Australia for providing guidance regarding hydrological modeling issues.

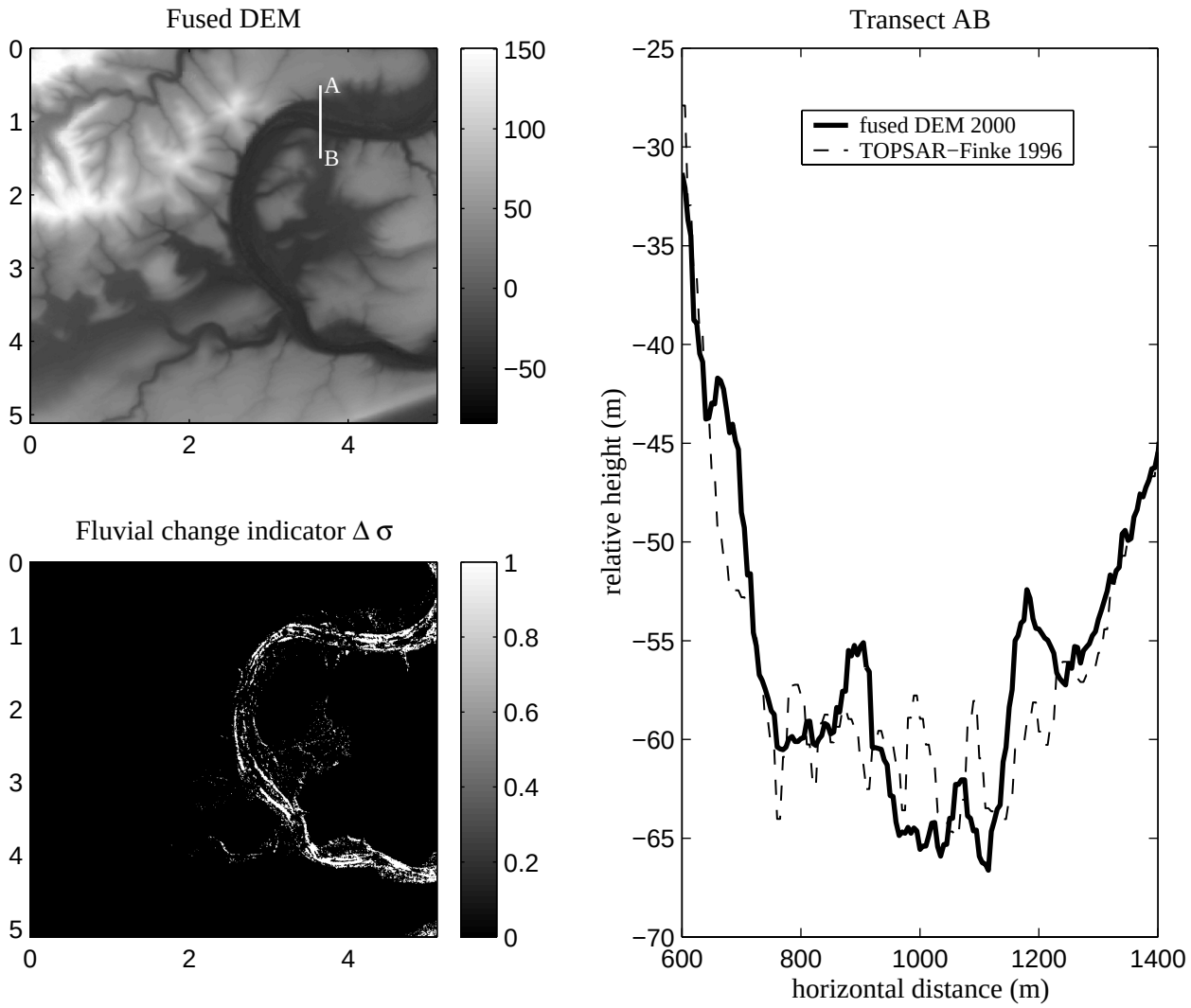

Fig. 8. Fluvial change in the Finke channel from 1996 to 2000, indicated by $\Delta\sigma$, and corresponding elevation transects.

7. APPENDIX A: MKS STOCHASTIC MODEL

Many natural processes, including topography, can exhibit approximately self-similar statistics across resolution scales. Statistical self similarity implies

$$x(\xi s) \stackrel{\mathcal{D}}{=} \xi^{\rho} x(s) \quad , 0 < \rho < 1 \quad , \xi > 0 \tag{8}$$

where ρ is the Hurst exponent, and $\stackrel{\mathcal{D}}{=}$ denotes equality in distribution [7]. An important class of statistically self-similar processes are $1/f$ processes [8]. $1/f$ processes are characterized by power spectra S_x that are proportional to $1/|f|^{\mu}$.

For most physical processes $0 \leq \mu \leq 2$ [8]. The value of μ effectively determines the rate of change of the process variability with spatial scale [9]. Fractional Brownian motion provides a useful characterization of $1/f$ processes that includes Brownian motion as a special case. Fractional Brownian motion is characterized by zero initial state and Gaussian statistics [5] [10].

For the linear dynamic model in (1), the stochastic detail is given by a white, Gaussian random variable with zero mean and variance $\Gamma^2(m)$, which can be a function of scale. In a multiscale $1/f$ model, the coarse-to-fine state transition operator is unity ($\Phi(s) = 1$), which indicates that the unforced state is perfectly correlated through scale [5]. All of the variation is provided by the stochastic detail function Γ. A multiscale $1/f^{\mu}$ process can be modeled in (1) with $\Gamma(m) = \Gamma_0\, 2^{(1-\mu)m/2}$, where Γ_0^2 is the variance at the root node. For $\mu > 1$, the variance decreases monotonically with increasing resolution.

Because a $1/f$ process implies are particular form for the power spectrum, mu and Γ_0 can be chosen so that the power spectrum of the multiscale data model matches the power spectrum of the observations. In our case, the power spectrum of the INSAR data is computed at the finest scale at which INSAR data are available. The power spectrum of a realization of the stochastic data model in (1) is computed at the same scale using empirically chosen values of μ and Γ_0 that produce a close match.

Power spectra of discrete image data can only represent signal energy over a finite range of spatial frequencies, so a 2-D Hamming window is applied to the data prior to computing the power spectra to reduce aliasing. Integrability of the power spectrum is maintained at high frequencies because of the bound on f due to discrete image data. Physical processes, such as topography, diverge from the $1/f$ model at very low frequencies, which leads to finite values for the power spectrum near $f = 0$.

8. APPENDIX B: MKS ALGORITHM

The MKS algorithm consists of an initialization step, followed by sweeps up and down the quadtree. *Initialization*
At the leaf nodes, enter the prior values

$$\hat{x}(s|s+) = 0 \tag{9}$$

$$P(s|s+) = P_s \tag{10}$$

Upward sweep
The upward sweep is equivalent to a Kalman filter operating in scale with an additional merge step that reduces the support of the estimates at each scale. Having defined the initial priors at the leaf nodes, the algorithm proceeds from the base of the quadtree up to the root node

$$\hat{x}(s|s) = \hat{x}(s|s+) + K(s)[y(s) - H(s)\hat{x}(s|s)] \tag{11}$$

$$P(s|s) = [I - K(s)H(s)]P(s|s+) \tag{12}$$

$$K(s) = P(s|s+)H^T(s)V^{-1}(s) \tag{13}$$

$$V(s) = H(s)P(s|s+)H^T(s) + R(s) \tag{14}$$

The project-ahead step is applied at all scales above the base. For $i = \{1, 2, 3, 4\}$, we have

$$\hat{x}(s|s\alpha_i) = F(s\alpha_i)\hat{x}(s\alpha_i|s\alpha_i) \tag{15}$$

$$P(s|s\alpha_i) = F(s\alpha_i)P(s\alpha_i|s\alpha_i)F^T(s\alpha_i) + Q(s\alpha_i) \tag{16}$$

The four project-ahead estimates from each 2×2 group of nodes at the previous scale must be merged into a single value at the current scale

$$\hat{x}(s|s+) = P(s|s+)\sum_{i=1}^{q} P^{-1}(s|s\alpha_i)\hat{x}(s|s\alpha_i) \tag{17}$$

$$P(s|s+) = \left[(1-q)P_s^{-1}(s) + \sum_{i=1}^{q} P^{-1}(s|s\alpha_i)\right]^{-1} \tag{18}$$

For the quadtree, $q = 4$.

Downward sweep
The upward estimate at the root node is used as the initial condition $\hat{x}^s(0) = \hat{x}(0|0)$ to start the downward sweep, where the superscript s refers to a smoothed quantity. The downward sweep then proceeds down the tree

$$\hat{x}^s(s) = \hat{x}(s|s) + J(s)[\hat{x}^s(Bs) - \hat{x}(Bs|s)] \quad (19)$$

$$P^s(s) = P(s|s) + J(s)[P^s(Bs) - P(Bs|s)]J^T(s) \quad (20)$$

$$J(s) = P(s|s)F^T(s)P^{-1}(Bs|s) \quad (21)$$

9. REFERENCES

[1] S. N. Madsen, J. M. Martin, and H. A. Zebker, "Analysis and evaluation of the NASA/JPL TOPSAR across-track interferometric SAR system," *IEEE Trans. Geosci. Remote Sensing*, vol. 33, pp. 383–391, Mar. 1995.

[2] J. Laferte, P. Perez, and F. Heitz, "Discrete Markov image modeling and inference on the quadtree," *IEEE Trans. Image Proc.*, vol. 9, no. 3, pp. 390–404, 2000.

[3] K. C. Chou, A. S. Willsky, and A. Benveniste, "Multiscale recursive estimation, data fusion, and regularization," *IEEE Trans. Automatic Control*, vol. 39, pp. 464–478, Mar. 1994.

[4] P. Kumar, "A multiple scale state-space model for characterizing subgrid scale variability of near-surface soil moisture," *IEEE Trans. Geosci. Remote Sensing*, vol. 37, pp. 182–197, Jan. 1999.

[5] P. W. Fieguth, W. C. Karl, A. S. Willsky, and C. Wunsch, "Multiresolution optimal interpolation and statistical analysis of TOPEX/POSEIDON satellite altimetry," *IEEE Trans. Geosci. Remote Sensing*, vol. 33, pp. 280–292, Mar. 1995.

[6] M. Daniel and A. Willsky, "A multiresolution methodology for signal-level fusion and data assimilation with applications to remote sensing," *Proc. IEEE*, vol. 85, pp. 164–180, Jan. 1997.

[7] M. Daniel and A. Willsky, "The modeling and estimation of statistically self-similar processes in a multiresolution framework," *IEEE Trans. Information Theory*, vol. 45, pp. 955–970, Apr. 1999.

[8] G. W. Wornell, "Wavelet-based representations for the $1/f$ family of fractal processes," *Proc. IEEE*, vol. 81, pp. 1428–1450, Oct. 1993.

[9] D. Evans, T. Farr, and J. van Zyl, "Estimates of surface roughness derived from synthetic aperture radar (SAR) data," *IEEE Trans. Geosci. Remote Sensing*, vol. 30, no. 2, pp. 382–389, 1992.

[10] R. Brown and P. Hwang, *Introduction to Random Signals and Applied Kalman Filtering*. New York, NY: Wiley, 3rd ed., 1997.

[11] G. Pickup and A. Marks, "Identification of floodplains and estimation of floodplain flow velocities for sediment transport modelling," *CSIRO Land and Water, Technical Report*, July 2001.

[12] D. Knightton, *Fluvial Forms and Processes*. New York, NY: Arnold, 1984.